NASA
Technical
Paper
2517
C.2
May 1986

Numerical Simulation of Scramjet Inlet Flow Fields

Ajay Kumar

NASA

NASA Technical Paper 2517

1986

Numerical Simulation of Scramjet Inlet Flow Fields

Ajay Kumar

Langley Research Center
Hampton, Virginia

NASA

National Aeronautics
and Space Administration

Scientific and Technical Information Branch

SUMMARY

A computer program has been developed to analyze supersonic combustion ramjet (scramjet) inlet flow fields. The program solves the three-dimensional Euler or Reynolds averaged Navier-Stokes equations in full conservation form by either the fully explicit or explicit-implicit, predictor-corrector method of MacCormack. Turbulence is modeled by an algebraic eddy-viscosity model. The analysis allows inclusion of end effects which can significantly affect the inlet flow field. Detailed laminar and turbulent flow results are presented for a symmetric-wedge corner, and comparisons are made with the available experimental results to allow assessment of the program. Results are then presented for two inlet configurations for which experimental results exist at the NASA Langley Research Center.

INTRODUCTION

For the past several years, a comprehensive research program has been under way at the NASA Langley Research Center to define and develop a viable air-breathing propulsion system for hypersonic flight applications. In this flight regime, a supersonic combustion ramjet (scramjet) engine becomes attractive. The scramjet engine concept being developed at Langley uses a fixed-geometry, rectangular module approach that integrates with the vehicle. (See refs. 1 and 2.) Use of fixed geometry reduces weight and system complexity, whereas the integration of the vehicle and propulsion system takes advantage of forebody compression to reduce inlet size and takes advantage of afterbody expansion to provide a low-drag, high-area-ratio exhaust nozzle. The basic modular concept that served as an initial focus of research in scramjet technology at Langley is shown in figure 1 with a sidewall removed. The inlet of this module compresses the flow with the swept, wedge-shaped sidewalls. The sweep of these sidewalls, in combination with the aft placement of the cowl on the underside of the engine, allows for efficient spillage and for good inlet starting characteristics over a range of operating Mach numbers with fixed geometry. The inlet compression is completed by three wedge-shaped struts (see cross-sectional view in fig. 1) which also provide locations for the injection of gaseous fuel. Considerable aerodynamic testing of this module has resulted in a baseline inlet design that performs well over a wide range of Mach numbers. The basic design features of this inlet are described in reference 3.

Because of possible diversified applications of scramjet engines, the inlet research is now moving into the investigation of several new concepts (ref. 4) which retain the basic features of the baseline design, such as fixed geometry, sweep, struts, and cutback cowl. However, most of this research has necessarily been experimental because of the complex nature of the inlet flow field, which is highly three dimensional, possibly turbulent, and has complex shock-wave/expansion-wave interactions. It also involves strong shock-wave/boundary-layer interactions which result in separated regions. Further, because of the aft placement of the cowl, a portion of the inlet flow field is exposed to the outside flow field ahead of the cowl. This exposure results in a significant interaction between the inside and outside flow. As a result of the aforementioned flow complexities and limitations on available computer systems, most scramjet inlet design in the past has had little analytical support. In recent years, however, the development of large-scale scientific computer systems has resulted in rapid progress in the field of computational

fluid dynamics. With the availability of large-storage, high-speed computers and advanced numerical algorithms, it is now feasible to calculate many complex two- and three-dimensional problems that could not be calculated previously. (See ref. 5.) Development and intelligent use of such analytical capabilities can be very helpful in eliminating the inefficient designs and in allowing promising design configurations to be developed with less reliance on extensive wind-tunnel testing.

An effort to provide an inlet analysis tool started with the development of a two-dimensional code (ref. 6) which solves the two-dimensional Euler or Navier-Stokes equations in conservation form. This two-dimensional code can also be used in a quasi-three-dimensional sense for the class of scramjet inlets shown in figure 1, with the assumptions that the shock waves in the inlet do not detach and the end effects are neglected. (See ref. 6.)

The purpose of the ongoing analysis is to develop a fully three-dimensional code for analyzing actual inlet configurations without simplifying assumptions. Results of the inviscid, three-dimensional analysis of scramjet inlet flow fields are presented in reference 7. This report describes the development and results from a three-dimensional viscous flow code that uses the full Reynolds averaged Navier-Stokes equations in conservation form as the governing equations. The equations in the physical domain are transformed to a regular computational domain by using an algebraic coordinate transformation that generates a set of boundary-fitted curvilinear coordinates (ref. 8). The transformed equations are solved by either the explicit (ref. 9) or explicit-implicit (refs. 10 and 11) predictor-corrector method of MacCormack. These methods are highly efficient on the vector processing computers for which the present code was developed.

The code in its present form can be used to analyze inviscid and viscous (laminar and turbulent) flows. In the case of turbulent flows, an algebraic, two-layer, eddy-viscosity model of Baldwin and Lomax (ref. 12) is used to estimate the turbulent viscosity. To verify the code, calculations are made for laminar and turbulent flow in a 9.48° symmetric-wedge corner at a Mach number of 3. The flow situation encountered in this problem is representative of the type of flow inside a scramjet inlet module. The results of the corner flow calculations are compared with the experimental data by West and Korkegi in reference 13. Detailed results are then presented for several inlet configurations for which experimental results are available. All inlet calculations account for the interaction between the internal and external flow ahead of the cowl. Results of the present calculations are compared with the available experimental results.

SYMBOLS

$B_{11} \ldots B_{33}$ metric data, given by equations (4)

c_p specific heat at constant pressure

c_v specific heat at constant volume

e total internal energy per unit volume

g throat gap

H_1 height of inlet

J	Jacobian determinant of transformation matrix
k	equivalent heat transfer coefficient
M	Mach number
N_{Pr}	Prandtl number
p	pressure
$\dot{q}$	heat flux
R	gas constant
T	temperature
t	time
u,v,w	velocity components in x-, y-, and z-directions
W	width of inlet
x,y,z	Cartesian coordinates
x_c	axial cowl location
x_t	axial throat location
δ_s	sidewall compression angle
Λ	sweep angle
μ	viscosity
ξ,η,ζ	transformed coordinates
ρ	density
τ	stress tensor

Subscripts:

ℓ	laminar
t	turbulent
w	wall
x	x-direction
y	y-direction
z	z-direction

∞	free stream
1	conditions at face of inlet

ANALYSIS

Governing Equations

The inlet flow field is described by the three-dimensional (3-D), Reynolds averaged Navier-Stokes equations in conservation form. These equations in the Cartesian coordinate system can be written as

$$\frac{\partial U}{\partial t} + \frac{\partial F}{\partial x} + \frac{\partial G}{\partial y} + \frac{\partial H}{\partial z} = 0 \tag{1}$$

where

$$U = \begin{bmatrix} \rho \\ \rho u \\ \rho v \\ \rho w \\ e \end{bmatrix}$$

$$F = \begin{bmatrix} \rho u \\ \rho u^2 - \tau_{xx} + p \\ \rho uv - \tau_{xy} \\ \rho uw - \tau_{zx} \\ ue - u\tau_{xx} - v\tau_{yx} - w\tau_{zx} + up + \dot{q}_x \end{bmatrix}$$

$$G = \begin{bmatrix} \rho v \\ \rho uv - \tau_{xy} \\ \rho v^2 - \tau_{yy} + p \\ \rho vw - \tau_{yz} \\ ve - u\tau_{yx} - v\tau_{yy} - w\tau_{zy} + vp + \dot{q}_y \end{bmatrix}$$

$$H = \begin{bmatrix} \rho w \\ \rho uw - \tau_{xz} \\ \rho vw - \tau_{yz} \\ \rho w^2 - \tau_{zz} + p \\ we - u\tau_{xz} - v\tau_{yz} - w\tau_{zz} + wp + \dot{q}_z \end{bmatrix}$$

Here, e is the total internal energy per unit volume and is given by $e = \rho\left[c_v T + (u^2 + v^2 + w^2)/2\right]$. The stress and flux terms used in equation (1) are given by

$$\left.\begin{aligned} \tau_{xx} &= 2\mu\left(\frac{\partial u}{\partial x} - \frac{\Delta}{3}\right) \\ \tau_{yy} &= 2\mu\left(\frac{\partial v}{\partial y} - \frac{\Delta}{3}\right) \\ \tau_{zz} &= 2\mu\left(\frac{\partial w}{\partial z} - \frac{\Delta}{3}\right) \\ \tau_{xy} &= \tau_{yx} = \mu\left(\frac{\partial u}{\partial y} + \frac{\partial v}{\partial x}\right) \\ \tau_{xz} &= \tau_{zx} = \mu\left(\frac{\partial u}{\partial z} + \frac{\partial w}{\partial x}\right) \\ \tau_{yz} &= \tau_{zy} = \mu\left(\frac{\partial w}{\partial y} + \frac{\partial v}{\partial z}\right) \\ \dot{q}_x &= -k\frac{\partial T}{\partial x} \\ \dot{q}_y &= -k\frac{\partial T}{\partial y} \\ \dot{q}_z &= -k\frac{\partial T}{\partial z} \end{aligned}\right\} \qquad (2)$$

where

$$\Delta = \frac{\partial u}{\partial x} + \frac{\partial v}{\partial y} + \frac{\partial w}{\partial z}$$

$$\mu = \mu_\ell + \mu_t$$

$$k = c_p\left(\frac{\mu_\ell}{N_{Pr,\ell}} + \frac{\mu_t}{N_{Pr,t}}\right)$$

To complete the set of governing equations, the equation of state ($p = \rho RT$) is used. The laminar viscosity μ_ℓ is calculated from Sutherland's law. The turbulent viscosity μ_t is estimated from an algebraic, eddy-viscosity model (Baldwin and Lomax) described in reference 12.

The governing equations are transformed by an algebraic coordinate transformation to a body-fitted coordinate system $\xi(x,y,z)$, $\eta(x,y,z)$, and $\zeta(x,y,z)$. The transformed governing equations in conservation form can be written as

$$\frac{\partial U'}{\partial t} + \frac{\partial F'}{\partial \xi} + \frac{\partial G'}{\partial \eta} + \frac{\partial H'}{\partial \zeta} = 0 \tag{3}$$

where

$$U' = JU$$

$$F' = B_{11}F + B_{21}G + B_{31}H$$

$$G' = B_{12}F + B_{22}G + B_{32}H$$

$$H' = B_{13}F + B_{23}G + B_{33}H$$

Here, $B_{11}\ldots B_{33}$ and the Jacobian matrix J are referred to as metric data and are defined as

$$J = x_\xi B_{11} + x_\eta B_{12} + x_\zeta B_{13} \tag{4a}$$

$$B_{11} = J\xi_x = y_\eta z_\zeta - y_\zeta z_\eta \tag{4b}$$

$$B_{12} = J\eta_x = y_\zeta z_\xi - y_\xi z_\zeta \tag{4c}$$

$$B_{13} = J\zeta_x = y_\xi z_\eta - y_\eta z_\xi \tag{4d}$$

$$B_{21} = J\xi_y = x_\zeta z_\eta - x_\eta z_\zeta \tag{4e}$$

$$B_{22} = J\eta_y = x_\xi z_\zeta - x_\zeta z_\xi \tag{4f}$$

$$B_{23} = J\zeta_y = x_\eta z_\xi - x_\xi z_\eta \tag{4g}$$

$$B_{31} = J\xi_z = x_\eta y_\zeta - x_\zeta y_\eta \tag{4h}$$

$$B_{32} = J\eta_z = x_\zeta y_\xi - x_\xi y_\zeta \tag{4i}$$

$$B_{33} = J\zeta_z = x_\xi y_\eta - x_\eta y_\xi \tag{4j}$$

These metric data are determined by using an algebraic grid generation technique with linear connecting functions. (See ref. 8.) A mesh refinement function described by Roberts in reference 14 is incorporated into the transformation in the y- and z-coordinate directions to concentrate more points near the boundaries in the physical domain. This function permits the mesh to be either refined near one boundary only or refined equally near both boundaries. Mesh refinement is required for better resolution of the boundary-layer region, but it is desirable even near the symmetry boundaries, where the flow is predominantly inviscid. It reduces the errors in the application of approximate boundary conditions, as used in the present code, especially in the region where a shock wave is interacting with the boundary.

Methods of Solution

The transformed governing equations are solved by the second-order accurate explicit (ref. 9) or explicit-implicit (ref. 10), predictor-corrector, time-dependent, finite-difference method of MacCormack. In these methods, if a solution to equation (3) is known at some time, $t = n\,\Delta t$, the solution at the next time, $t = (n + 1)\,\Delta t$, can be obtained from

$$U'^{\,n+1}_{i,j} = L(\Delta t)\; U'^{\,n}_{i,j}$$

for each grid point (i,j). The finite-difference operator L consists of a predictor step and a corrector step which can be written in functional form as follows:

$$U'^{\overline{n+1}} = f(U'^{n})$$

$$U'^{n+1} = f\left(U'^{n}, U'^{\overline{n+1}}\right)$$

For the explicit-implicit method, each step contains two stages. The first stage uses the explicit method, which is subject to restrictive explicit stability conditions. The second stage removes these stability conditions by numerically transforming the equations of the first stage into an implicit form. For the explicit method, each step has only the explicit stage. The details of the methods are given in references 9 and 10. Reference 11 provides some helpful observations for successfully using the explicit-implicit method. In the present code, the implicit stage is added only in the y- and z-coordinate directions, assuming that the spatial discretization in these directions is much more refined than in the axial direction (x-coordinate).

The preceding methods are well-suited for the vector-processing computers, because they allow a high degree of vectorization. A fourth-order numerical damping of the type used in reference 6 is required for damping the oscillations which occur in the neighborhood of strong shocks in the flow.

Boundary and Initial Conditions

The flow variables at the inflow boundary are held fixed at prescribed conditions, whereas, extrapolation from interior grid points is used to obtain the flow variables at the outflow boundary. No-slip and adiabatic wall or known wall temperature conditions are used on the solid boundaries. The wall pressure is determined from the approximation where the normal derivative of pressure vanishes. On the open boundaries, extrapolation from interior grid points is used. If the flow is symmetric about a plane, only half the flow field is calculated, and symmetry boundary conditions are imposed.

The boundary conditions are applied in both the predictor and corrector steps. Initial conditions are normally prescribed for each set of calculations by assuming that free-stream conditions exist at all the grid points except at the boundaries where proper boundary conditions are applied.

Convergence

To check the convergence to steady state, the percentage change in density during a time-step is calculated at each grid point in the flow. If this change is less than a prescribed number at all the grid points, the calculation is assumed to be converged. However, in many cases, the change in density may not be reduced below the prescribed value at all the points; instead, it may assume a certain asymptotic value. For those cases, the calculation is terminated based on a physical time-convergence criterion. For this criterion, the calculations are stopped when the equations have been relaxed in time equal to that required by the free stream to

traverse the flow domain approximately three times. Although this criterion is empirical in nature, it has been found to work well for most supersonic flow problems.

PROGRAM ORGANIZATION AND COMPUTER REQUIREMENTS

The present code was originally written for the Control Data CYBER 203 vector-processing computer system at NASA Langley. It has now been upgraded to the VPS-32 computer. The VPS-32 computer has 16 million 64-bit words of primary memory, but the virtual memory feature of the system allows a program to have a data base larger than the available primary memory. The memory of the computer is divided into pages. These pages are available in two sizes. The small page has 8192, 64-bit words, and the large page has 65 536, 64-bit words, or 8 small pages. When the code refers to some information that is not resident in the primary memory, the page that has not been used for the longest time moves out from the primary memory to accommodate the required page from virtual memory. This process is called "paging" and is very slow compared with the speed of the central processing unit (CPU) because of hardware limitations of the system. With a large data-base program, unless considerable effort is made to manage both the data and the associated computational procedures, a situation can occur where the machine is spending more time moving pages of data in and out of primary memory than on actual computations. This situation is especially true with the numerical technique used in the present analysis, where the program goes through the entire data base several thousand times. In this situation, it is advisable to avoid the use of virtual memory. By proper program organization, it is possible to keep the storage required by the temporary variables to a minimum, so that more grid points can be used for discretizing the flow domain without the use of virtual memory.

Another feature of vector processors is that they can achieve high operation rates when a large degree of vectorization is present in the computation (i.e., when an identical operation is being performed on consecutive elements in the memory). The operation rate increases as the length of the vector increases. The present code is organized in such a way that calculations are made in planes perpendicular to one of the coordinate directions with vector length approximately equal to the number of grid points in a plane. This arrangement allows efficient use of the vector-processing capability of the computer. Temporary reusable vectors are maintained in only two local planes. When only the explicit method was being used in the code, it was possible to start the corrector step in plane I - 1 once the predictor step was completed in plane I - 1 and I as shown in figure 2. However, with the implementation of the explicit-implicit method, the predictor step must be completed first in all planes before starting the corrector step, thus resulting in more storage requirements than with the fully explicit method.

One more consideration which significantly impacts the number of grid points available for flow discretization is the way in which the metric data are provided to the main flow program. Normally, the metric data are calculated and stored for use in the main program, but this approach requires ten 3-D arrays for the metric data given in equations (4) and results in a significant increase in the number of 3-D arrays. An alternative approach is to input x-, y-, and z-coordinates to the main program and to calculate the metric data plane by plane in each time-step. This approach, although it increases the execution time slightly, requires only three 3-D arrays and ten 2-D arrays. The present code uses the second approach, which increased the number of grid points that can be stored in the main memory of the computer by about 40 percent. The code now requires seventeen 3-D arrays and many 2-D arrays.

The code as such uses CYBER 200 FORTRAN language with 32-bit-word arithmetic. Use of 32-bit-word arithmetic increased the primary memory to 32 million words and reduced the execution time by a factor of over 2 without adversely affecting the accuracy of the results. The maximum grid size that can be computed with this code without going out of primary memory is approximately 1.4 million points. The compute rate of the code is about 0.7×10^{-5} sec/grid point/time-step; therefore, the code requires about 1 hour to compute 1000 time-steps on a grid of 0.5×10^{6} points.

DISCUSSION OF RESULTS

Results are presented for a symmetric-wedge corner and two scramjet inlet configurations. Comparisons are made with the available experimental results to allow assessment of the present analysis.

Results for Symmetric-Wedge Corner

To verify the computer program, calculations are made for laminar and turbulent flow in a 3-D, 9.48° symmetric-wedge corner (fig. 3) for which detailed experimental results are available. The flow in such a corner is representative of the type of flow inside a scramjet inlet. A schematic of the basic characteristics of the corner flow is shown in figure 3. It has a very complex structure that includes wall shocks, corner shock, internal shocks, and slip lines. To predict such a complex flow field, it is necessary to properly discretize the corner geometry. In the present analysis, a grid of 39 × 61 × 61 points (39 points in the x-direction, 61 points in the y-direction, and 61 points in the z-direction) is used with suitable refinement near the corner walls, based on the flow Reynolds number. Calculations are made for the case with $M_\infty = 3.0$, $T_\infty = 105$ K, and $T_w = 294$ K. In the case of laminar flow, the free-stream pressure is 1095 Pa, and the Reynolds number is 0.39×10^{6}. Figure 4 shows the details of the corner flow structure as calculated by the present analysis and compared with the results of reference 13. Plotted in this figure are the calculated and the experimentally determined density contours. The calculations have predicted the corner flow features very well and are in very good agreement with the experiment.

A comparison of the sidewall pressure distribution with experiment is shown in figure 5. Again, the predicted results compare well with the experimental results.

In the case of turbulent flow, calculations are made at a free-stream pressure of 3000 Pa and a Reynolds number of 1.1×10^{6}. The experimental results in reference 13 show that the flow in the corner is fully turbulent at this Reynolds number and that there is very little change in the flow structure for Reynolds numbers in the range of 1.1×10^{6} to 60×10^{6}. Since the computational requirements are much less severe at 1.1×10^{6} than at 60×10^{6}, the calculations are made at 1.1×10^{6}. Figure 6 shows the comparison of the surface pressure distribution with the experiment. The present results are in very good agreement with the experimental results.

Results for Scramjet Inlet

Detailed results are now presented for a parametric scramjet inlet and a single-strut, reverse-sweep, scramjet inlet. All calculations are made with a grid of 65 × 31 × 51 points. Since the inlets are symmetric about the x-z plane, only half

the inlet flow is calculated. Out of the 51 points in the z-direction, 15 points are located under the cowl to account for the end effects. As mentioned previously, these end effects arise because of the aft placement of the cowl, which exposes the inlet flow to the outside flow ahead of the cowl closure. Figure 7 shows the side view of an inlet module with 0° sweep and wedge-shaped sidewalls. A cross-sectional view is also shown in the figure. The flow that has been processed by the sidewall shock inside the inlet is at a higher pressure than that outside the inlet. This pressure differential causes an expansion wave to run into the inlet, and an induced flow is created in the downward direction that results in some flow spillage in addition to that caused by any sidewall sweep. To account for these end effects in the analysis, a portion of the flow under the cowl must be included, but the problem is to decide how much more of the flow field needs to be included. Ideally, one should go down and around the sidewalls far enough so that the free-stream conditions can be applied on the free boundaries, but this would greatly increase the computational requirements. In the present analysis, the region is extended, as shown in figure 7 by dashed lines. Extrapolation from interior grid points is used all along the dashed-line boundaries except at the inflow boundary, where the flow conditions are prescribed.

Results for the parametric inlet are presented first, followed by the single-strut, reverse-sweep inlet results.

Parametric Inlet

The present analysis has been used to calculate the flow field in the inlet of a parametric scramjet engine designed for experimental studies at the Langley Research Center. Figure 8 shows the geometry of the engine. The inlet sidewalls are swept back at angle Λ. As mentioned previously, the purpose of the sidewall sweep is to turn the flow downward, which results in some flow spilling out of the inlet ahead of the cowl plate. This provides the potential to operate over a range of Mach numbers with a fixed-geometry inlet. In other words, the sidewall sweep results in variable-geometry-like behavior with a fixed-geometry inlet. The sidewall sweep ends along line A-B, and the cowl closure starts at point B. The inlet is 7.2 in. high and about 30 in. long. The sidewalls have a 6° wedge angle. Various other dimensions and angles are also shown in the figure. In this configuration, sidewall sweep, cowl location, and geometric contraction ratio can be varied. It is also possible to add struts in the inlet, if necessary. These features make possible the evaluation of the influence of various geometric parameters on inlet performance over a range of Mach numbers. Experimental results have been obtained by Trexler of NASA Langley Research Center for the inlet flow field at Mach 3.5 and sidewall sweep angles of 0° to 45°.

To compare the numerical results with the experimental data, flow field is calculated at Mach 3.5 in the inlet with 0° sidewall sweep and a geometric contraction ratio W/g of 4. Figure 9 shows the details of this configuration. Pressure and temperature at the face of the inlet are 7230 Pa and 75.7 K. These values correspond to the experimental conditions. Calculations are made for inviscid, laminar, and turbulent flow in the inlet. The impact of the end effects in the calculations is discussed first with the help of inviscid results.

Figure 10 shows the sidewall pressure distribution at two axial locations. If the end effects were not included in the analysis, the sidewall pressure distribution at any given axial location should have remained constant at a certain value. Also, the inlet should have captured all the flow that entered it, since the sidewall sweep

is 0°. However, it is shown in figure 10 that at $x/H_1 = 1.25$, about 45 percent of the flow above the cowl plane is affected by the expansion wave. The pressure ratio in the cowl plane is reduced to 1.42 from 1.61. At $x/H_1 = 2.24$, the end effects extend to about 75 percent of the flow above the cowl plane. The pressure ratio in the cowl plane is reduced to 2.4 from 4.06. In addition, the calculation showed that the inlet spilled a significant amount of the flow because of the end effects. It is apparent from these results that the end effects have a very significant impact on the inlet flow and should be included in the analysis to accurately predict the inlet flow field.

The pressure contours and velocity vector field are shown in figures 11 and 12 for inviscid, laminar, and turbulent flow through the inlet. To illustrate the complexity of the flow, the pressure contours are displayed in figure 11 in a plane located at $z/H_1 = 0.5$. These plots clearly show the shock and expansion waves and their interactions with each other and with the boundaries. Also, the shock interaction points move slightly upstream in the case of viscous flows. Plots of velocity vector field in the aforementioned plane are shown in figure 12. For clarity, only the region between $x/H_1 = 1.486$ and 3.4 is shown in the figure. The laminar boundary layer separates at three places on the sidewall as a result of shock-wave/boundary-layer interaction. (See fig. 12(b).) The separation disappears for the turbulent flow under the present flow conditions, since the turbulent boundary layer is able to accept higher adverse pressure gradients without separating.

Figures 13 and 14 show the sidewall pressure distributions at two inlet height locations. Unpublished experimental results from Trexler are also shown. Only turbulent flow calculation results are plotted for comparison with the experiment. The flow in the region between $x/H_1 = 2.6$ and 3.5 is highly complex because of the interactions of sidewall shock, sidewall expansion, cowl shock, expansion due to the end effects, and induced shock due to boundary-layer separation. All these interactions are taking place in a region where the gap between the sidewalls is relatively small. The prediction is further complicated by pre-shock and post-shock oscillations introduced by the numerical method. Even with all these complexities, the predicted results agree reasonably well with the experimental data in both planes. The predicted pressure levels are, in general, slightly higher than those measured in the experiment. Some of this difference is due to the fact that the experimental Mach number is slightly lower than the 3.5 used in the present calculations.

As discussed previously, the flow captured by the inlet is an important quantity in its performance calculations. In the case of the present inlet configuration, there is no flow spillage due to sidewall sweep, because the sweep angle is zero. However, the end effects result in some spillage; therefore, there is a reduction in the amount of inlet capture. Present calculations for the turbulent flow predicted an inlet capture that is within 2 percent of the experimental value.

Although results are presented here for only one set of geometrical parameters, calculations have been made for several other sweep angles, geometrical contraction ratios, cowl locations, and inflow conditions. These results are discussed in detail in reference 15.

Single-Strut, Reverse-Sweep Inlet

Another inlet configuration that has been analyzed numerically is shown in figure 15. It has wedge-shaped sidewalls which are swept back at an angle of 30°. A compression strut is located in the center passage of the inlet, which is also swept,

but it is swept forward at an angle of 30°. The throat width is held constant at all heights in the inlet. As a result, the inlet throat has 0° sweep. An unswept throat may be an advantage in reducing the potential for adverse inlet combustor coupling. (See ref. 16.) The strut reduces the overall length of the inlet by providing additional compression surfaces. Opposite sweep of the strut and sidewalls is intended to reduce flow turning normal to the plane of the cowl; this reduction in downflow should help to reduce the strength of the internal cowl shock and to alleviate high pressure levels normally generated by the cowl shock. Reduced downflow also results in reduced spillage. The inlet has been tested in a Mach 4 tunnel at Langley by Trexler. Unpublished results from those tests are compared herein with the calculations. The following flow conditions are used in the analysis:

$$M_1 = 4.03; \quad p_1 = 8724 \text{ Pa}; \quad T_1 = 65 \text{ K}$$

These conditions correspond to the experimental conditions. The inlet for which the calculations are made has a geometric contraction ratio W/g of 4.16, and the cowl is located at the throat.

Figure 16 shows the pressure contours and figure 17 shows the velocity vector field in three planes corresponding to $z/H_1 = 0.145$, 0.5, and 0.89. One of the problems associated with single-strut inlets with similar sweep on the sidewalls and the strut is that for a given Mach number, the shock waves from the sidewalls and the strut coalesce into a stronger shock wave. This shock wave coalescence is not desirable for the operation of the inlet over a Mach number range with fixed geometry. In the present configuration, it appears that the shock-wave coalescence problem is alleviated. Because of the opposite sweep of the sidewalls and the strut, the shock waves may coalesce only in certain planes, not all across the inlet height, at a given Mach number. For example, figure 16 shows that for the present conditions, shock waves coalesce in the planes near the top surface but not in the planes near the cowl. The separated flow regions on the sidewalls in figure 17 also substantiate the preceding observation.

Sidewall static-pressure distributions are shown in figure 18. It is shown in this figure that the maximum pressure level is predicted in the middle plane rather than in the plane closer to the cowl. In the parametric inlet configuration discussed previously, maximum pressure was predicted in the plane closer to the cowl. Figure 18 also shows that the predicted pressure levels compare well with the experimental results up to the inlet throat. There are deviations downstream of the throat because the experimental model has significantly different geometry than that used in the present calculations.

The predicted inlet capture is within 2 percent of the experimental value for this inlet configuration, also.

CONCLUDING REMARKS

A computer program has been developed to numerically calculate the complex, three-dimensional flow field in supersonic combustion ramjet (scramjet) inlets. The program solves the three-dimensional Euler or Navier-Stokes equations in full conservation form by either the fully explicit or explicit-implicit, predictor-corrector method of MacCormack. Turbulence is modeled by an algebraic eddy-viscosity model.

An important feature of the program is that it allows inclusion of end effects in the inlet flow calculations. These end effects arise as a result of the interaction of the inlet flow with the external flow, and they affect the inlet flow field very significantly.

To assess the program, predicted laminar and turbulent flow results are compared with experiment for a 9.48° symmetric-wedge corner at Mach 3. Results are then presented for two inlet configurations. The results of these calculations are also compared with the available experimental results. In general, the program has predicted the flow field well. The effort is continuing to apply and validate the code for a wider range of conditions and for more practical inlet geometries.

NASA Langley Research Center
Hampton, VA 23665-5225
September 17, 1985

REFERENCES

1. Jones, Robert A.; and Huber, Paul W.: Toward Scramjet Aircraft. Astronaut. & Aeronaut., vol. 16, no. 2, Feb. 1978, pp. 38-48.

2. Beach, H. Lee, Jr.: Hypersonic Propulsion. Aeropropulsion 1979, NASA CP-2092, 1979, pp. 387-401.

3. Trexler, Carl A.; and Souders, Sue W.: Design and Performance at a Local Mach Number of 6 of an Inlet for an Integrated Scramjet Concept. NASA TN D-7944, 1975.

4. Trexler, C. A.; and Pinckney, S. Z.: Inlet Research for the Langley Airframe Integrated Scramjet. 1983 JANNAF Propulsion Meeting, Volume V, Karen L. Strange, ed., CPIA Publ. 370 (Contract N00024-83-C-5301), Appl. Phys. Lab., Johns Hopkins Univ., Feb. 1983, pp. 663-675.

5. Kumar, Ajay; Rudy, D. H.; Drummond, J. P.; and Harris, J. E.: Experiences With Explicit Finite-Difference Schemes for Complex Fluid Dynamics Problems on STAR-100 and CYBER-203 Computers. Paper presented at CYBER-205 Applications Symposium (Fort Collins, Colorado), Colorado State Univ., Aug. 1982.

6. Kumar, Ajay: Numerical Analysis of the Scramjet-Inlet Flow Field by Using Two-Dimensional Navier-Stokes Equations. NASA TP-1940, 1981.

7. Kumar, Ajay: Three-Dimensional Inviscid Analysis of the Scramjet Inlet Flow Field. AIAA-82-0060, Jan. 1982.

8. Smith, R. E.: Two-Boundary Grid Generation for the Solution of the Three-Dimensional Compressible Navier-Stokes Equations. NASA TM-83123, 1981.

9. MacCormack, Robert W.: The Effect of Viscosity in Hypervelocity Impact Cratering. AIAA Paper No. 69-354, Apr.-May 1969.

10. MacCormack, R. W.: A Numerical Method for Solving the Equations of Compressible Viscous Flow. AIAA-81-0110, Jan. 1981.

11. Kumar, Ajay: Some Observations on a New Numerical Method for Solving the Navier-Stokes Equations. NASA TP-1934, 1981.

12. Baldwin, Barrett; and Lomax, Harvard: Thin-Layer Approximation and Algebraic Model for Separated Turbulent Flows. AIAA Paper 78-257, Jan. 1978.

13. West, John E.; and Korkegi, Robert H.: Supersonic Interaction in the Corner of Intersecting Wedges at High Reynolds Numbers. AIAA J., vol. 10, no. 5, May 1972, pp. 652-656.

14. Roberts, Glyn O.: Computational Meshes for Boundary Layer Problems. Proceedings of the Second International Conference on Numerical Methods in Fluid Dynamics, Volume 8 of Lecture Notes in Physics, Maurice Holt, ed., Springer-Verlag, 1971, pp. 171-177.

15. Kumar, Ajay; and Trexler, Carl A.: Analysis and Protection of the Performance of Scramjet Inlets Utilizing a Three-Dimensional Navier-Stokes Code. 1984 JANNAF Propulsion Meeting, Volume V, Karen L. Strange, ed., CPIA Publ. 390, Vol. V (Contract N00024-83-C-5301), Appl. Phys. Lab., Johns Hopkins Univ., Feb. 1984, pp. 661-675.

16. Andrews, Earl H.; Northam, G. Burton; Torrence, Marvin G.; Trexler, Carl A.; and Pinckney, S. Zane: Mach 4 Wind-Tunnel Tests of a Hydrogen-Burning Airframe-Integrated Scramjet Engine. NASA TM-85688, 1984.

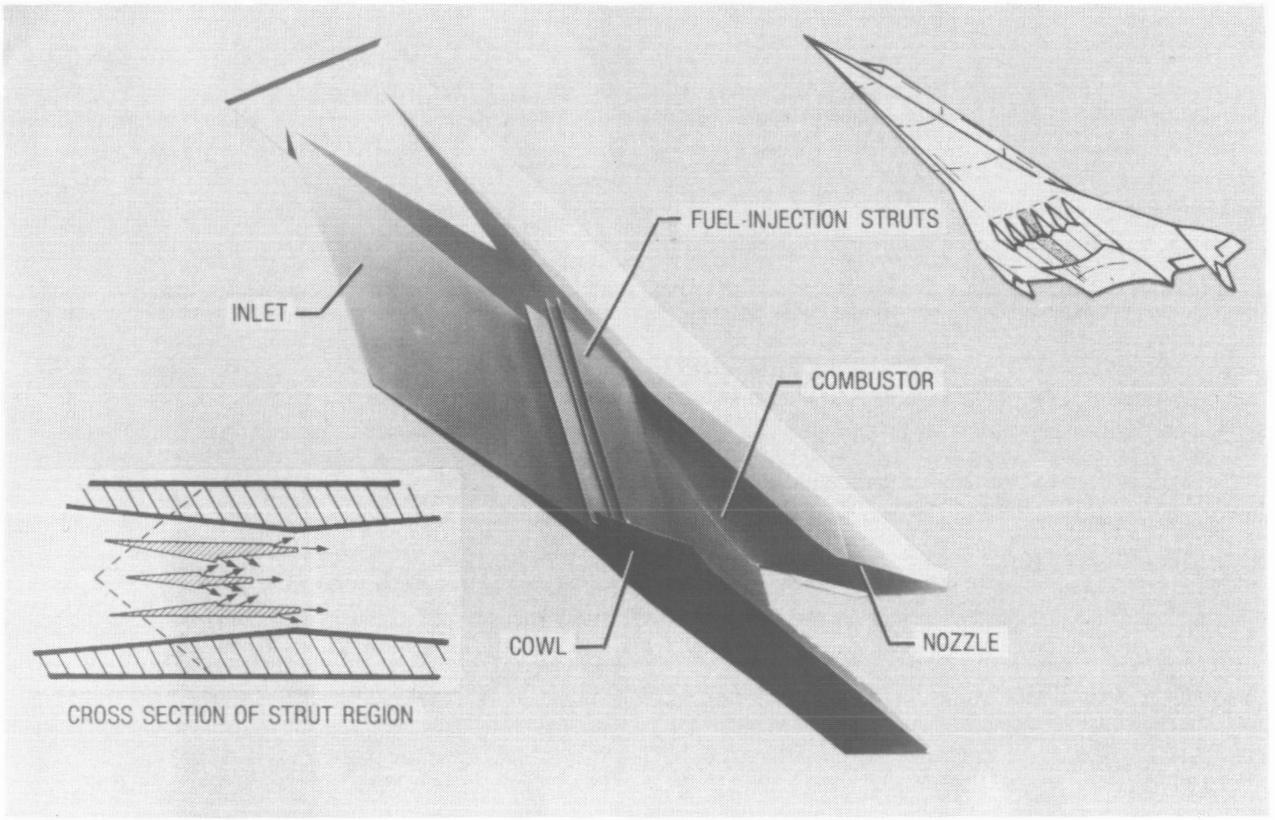

Figure 1.- Scramjet engine module and cross section.

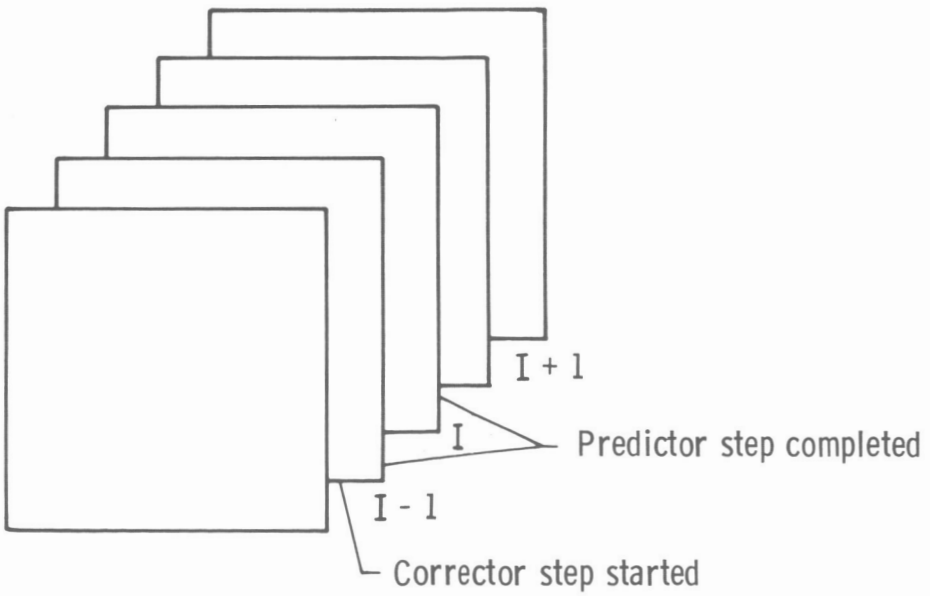

Figure 2.- Program organization of 3-D Navier-Stokes code.

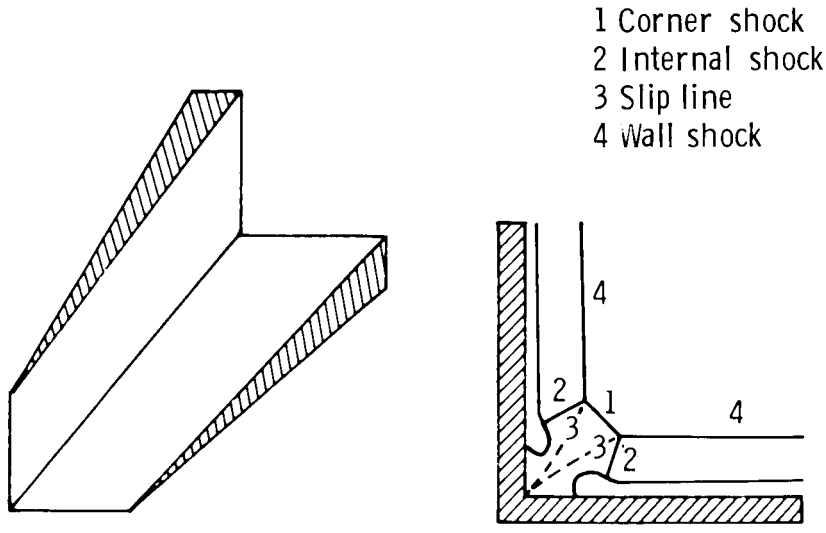

Figure 3.- Symmetric-wedge corner and schematic of corner flow.

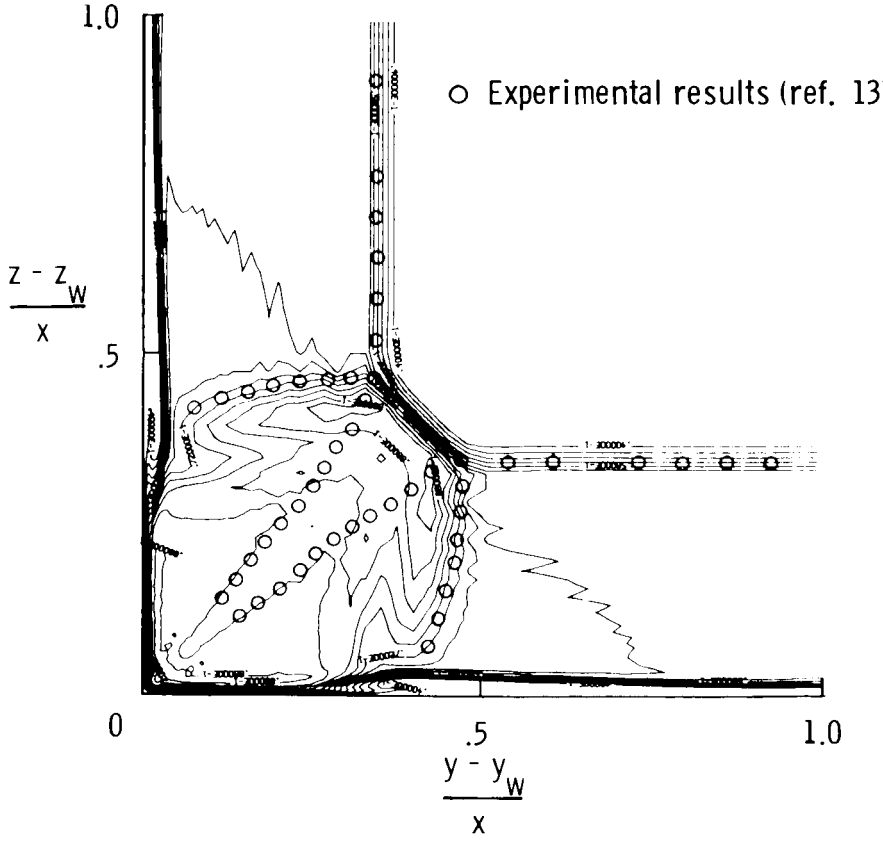

Figure 4.- Density contours for symmetric-wedge corner (laminar flow).

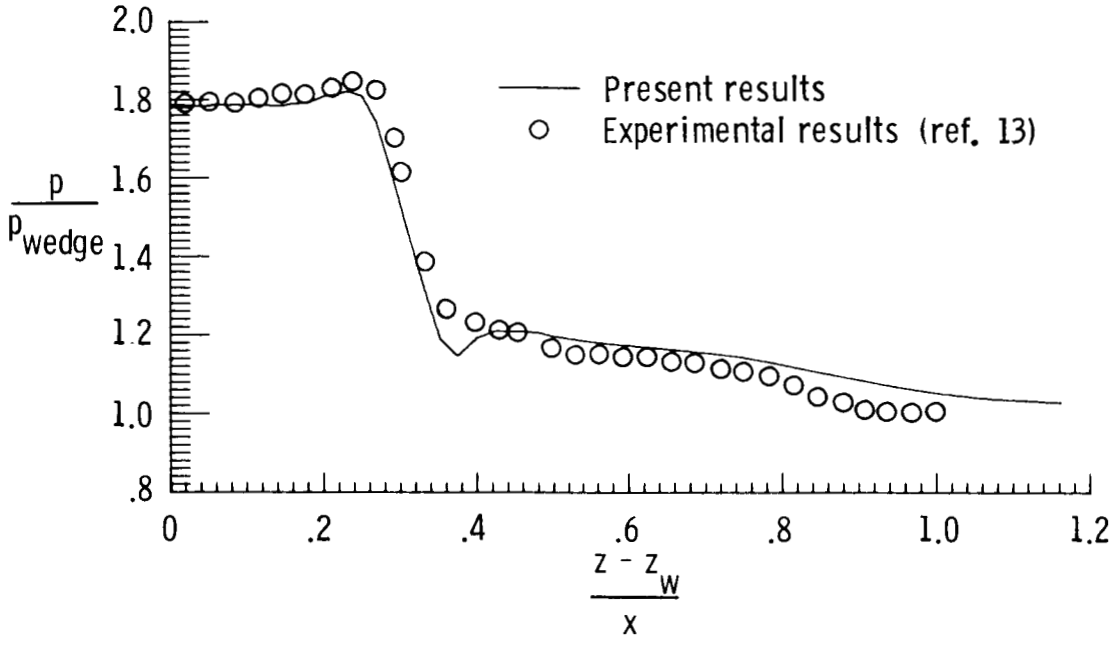

Figure 5.- Surface pressure distribution for symmetric-wedge corner (laminar flow).

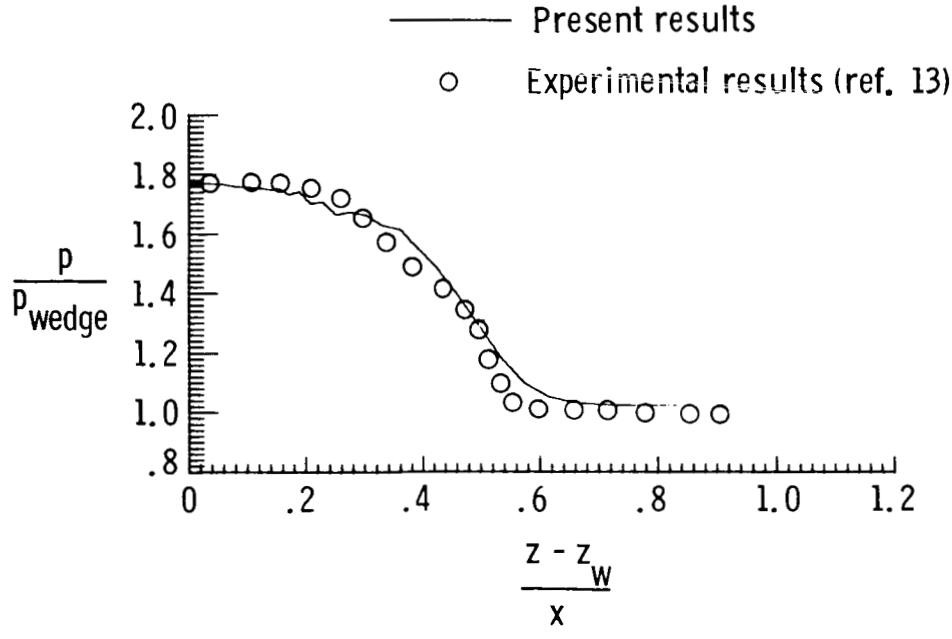

Figure 6.- Surface pressure distribution for symmetric-wedge corner (turbulent flow).

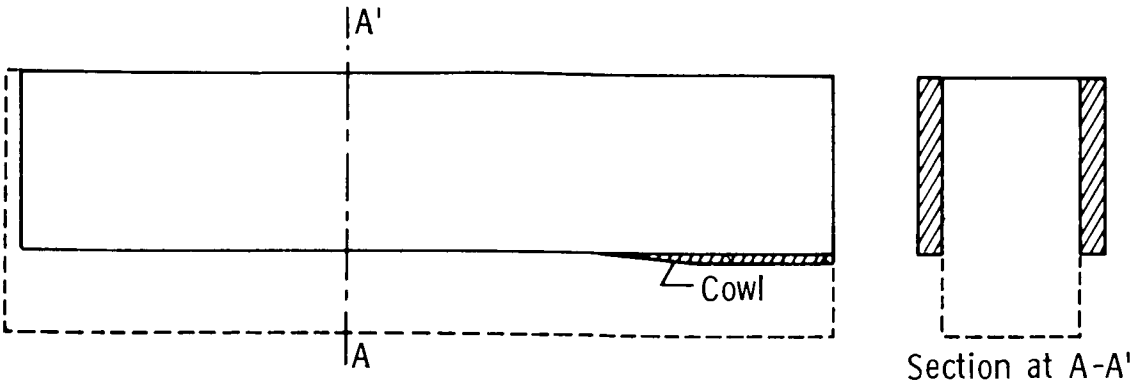

Figure 7.- Physical domain of computation for inclusion of end effects.

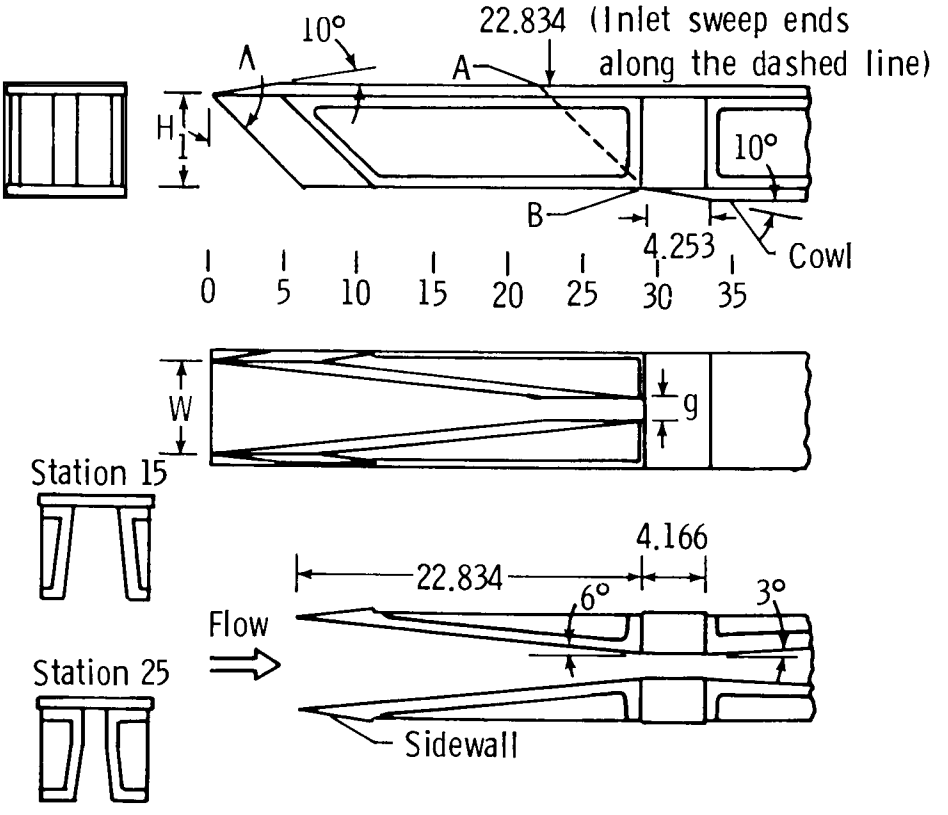

Figure 8.- Geometry of parametric scramjet engine.
(All linear dimensions are in inches.)

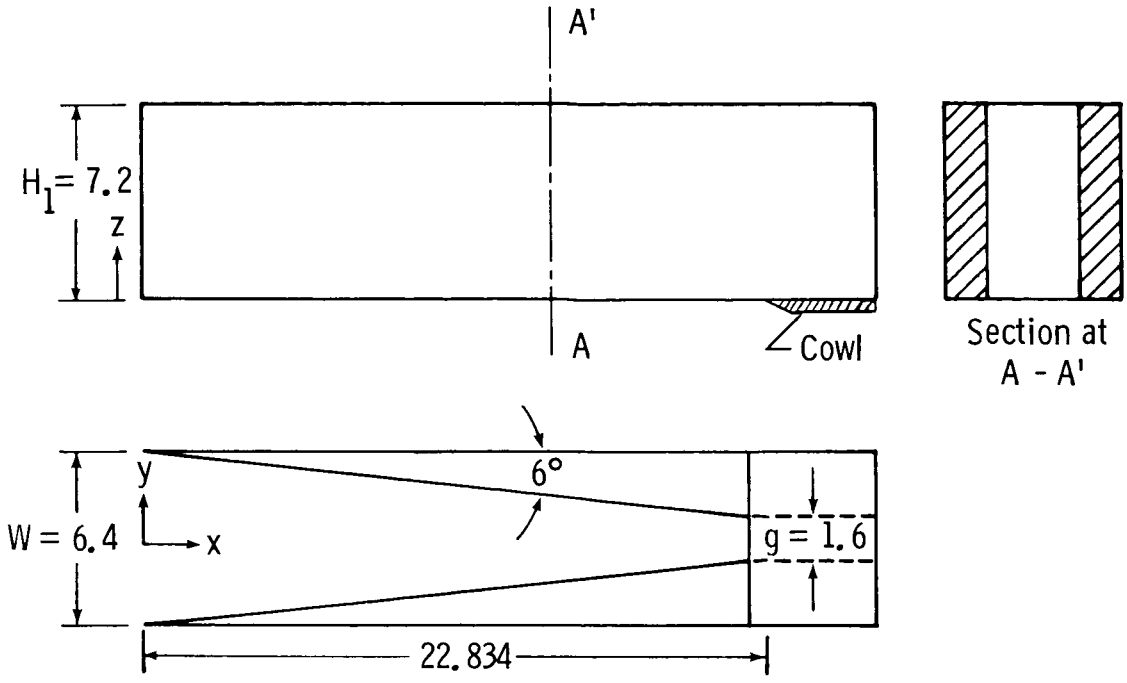

Figure 9.- Geometry of parametric inlet with $\Lambda = 0°$. (All linear dimensions are in inches.)

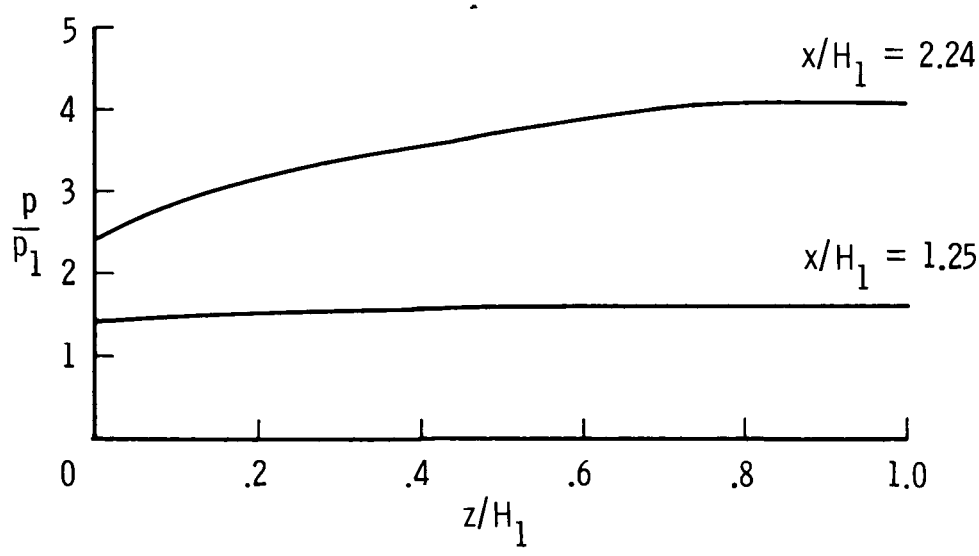

Figure 10.- Inviscid sidewall pressure distribution at two axial locations.

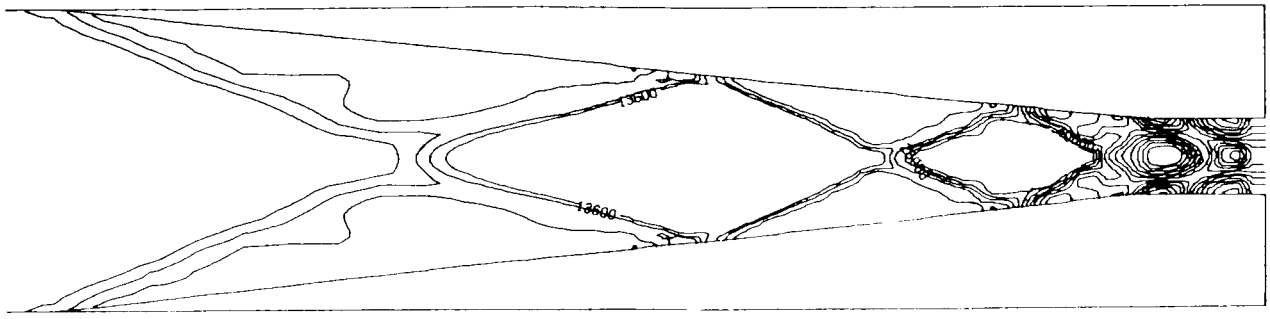

(a) Inviscid.

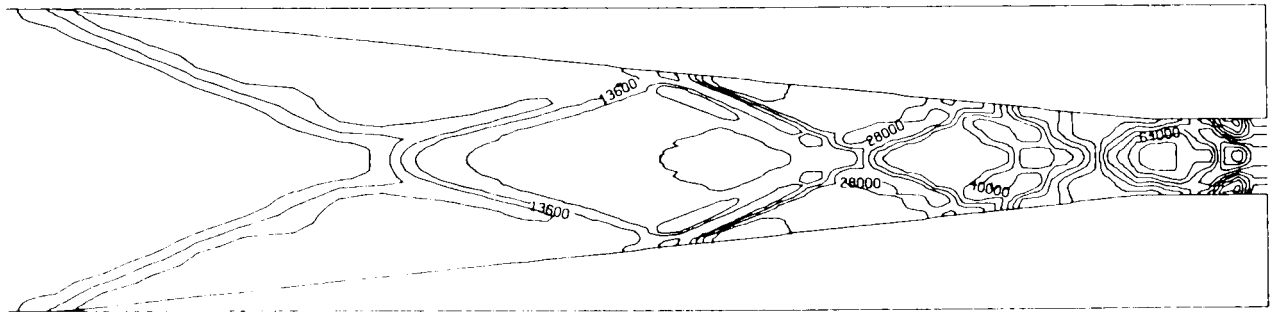

(b) Laminar.

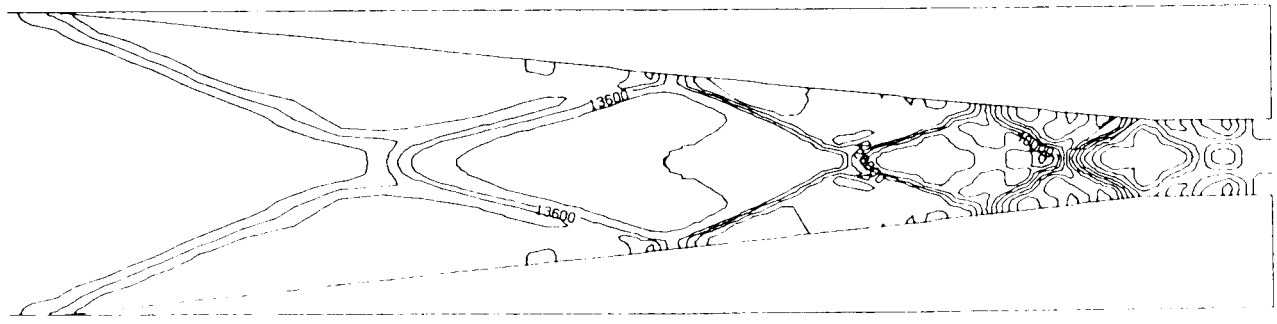

(c) Turbulent.

Figure 11.- Pressure contours in a plane located at $z/H_1 = 0.5$.

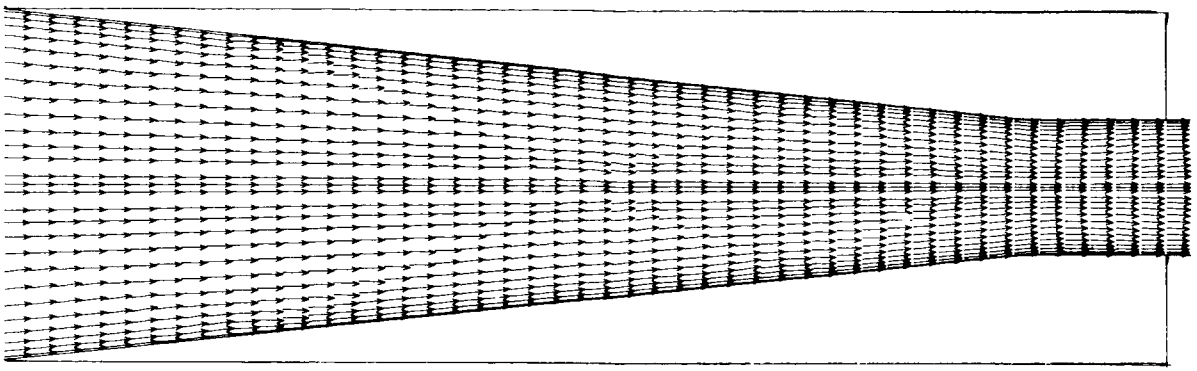

(a) Inviscid.

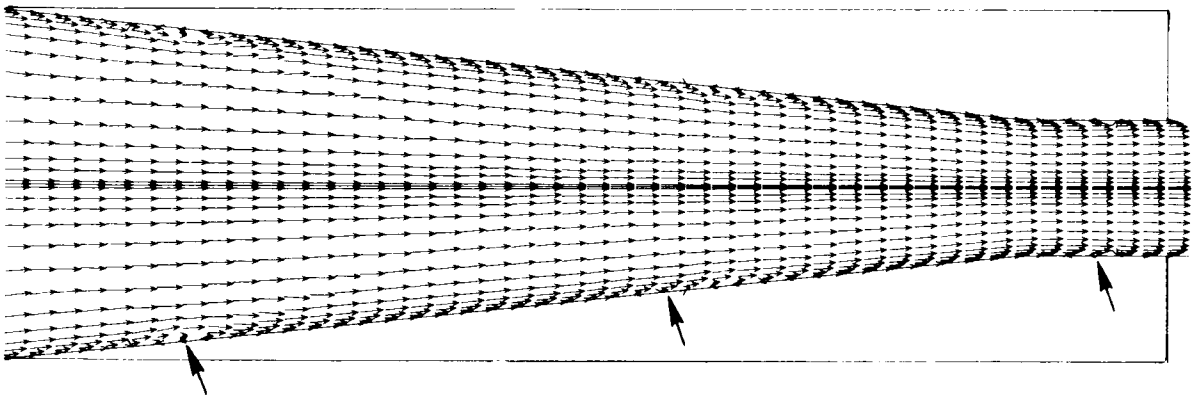

(b) Laminar.

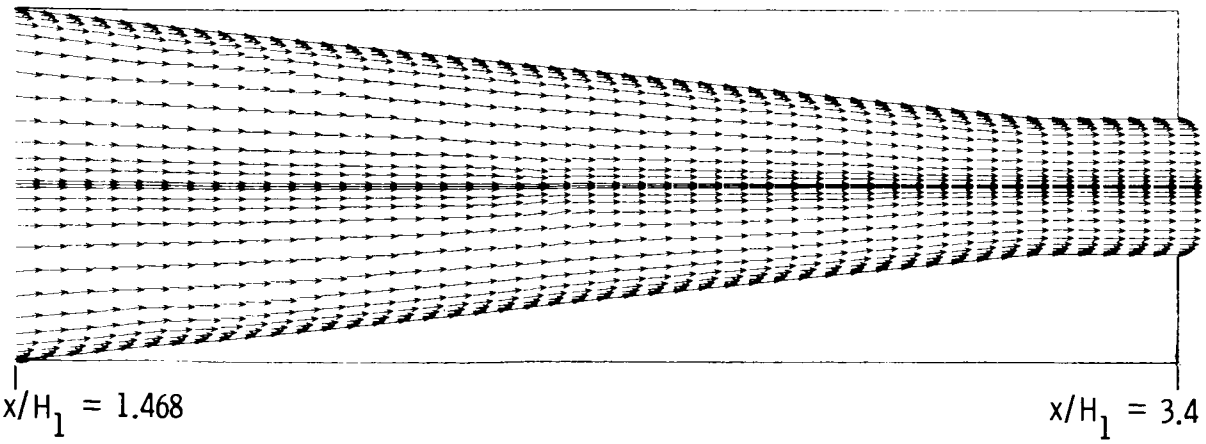

(c) Turbulent.

Figure 12.- Velocity vector field in a plane located at $z/H_1 = 0.5$.

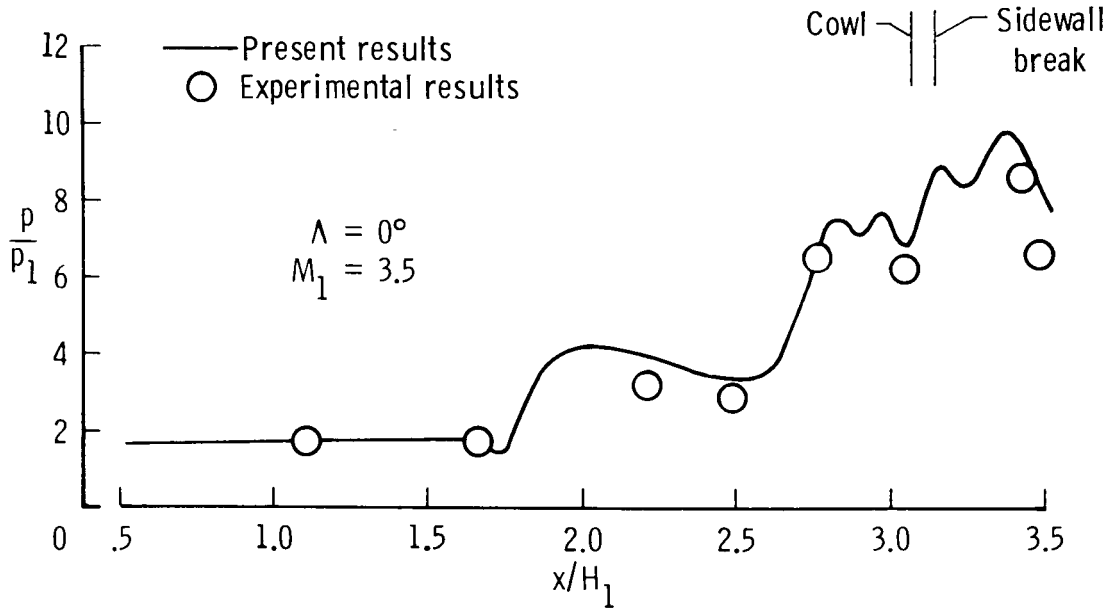

Figure 13.- Sidewall pressure distribution at $z/H_1 = 0.5$.

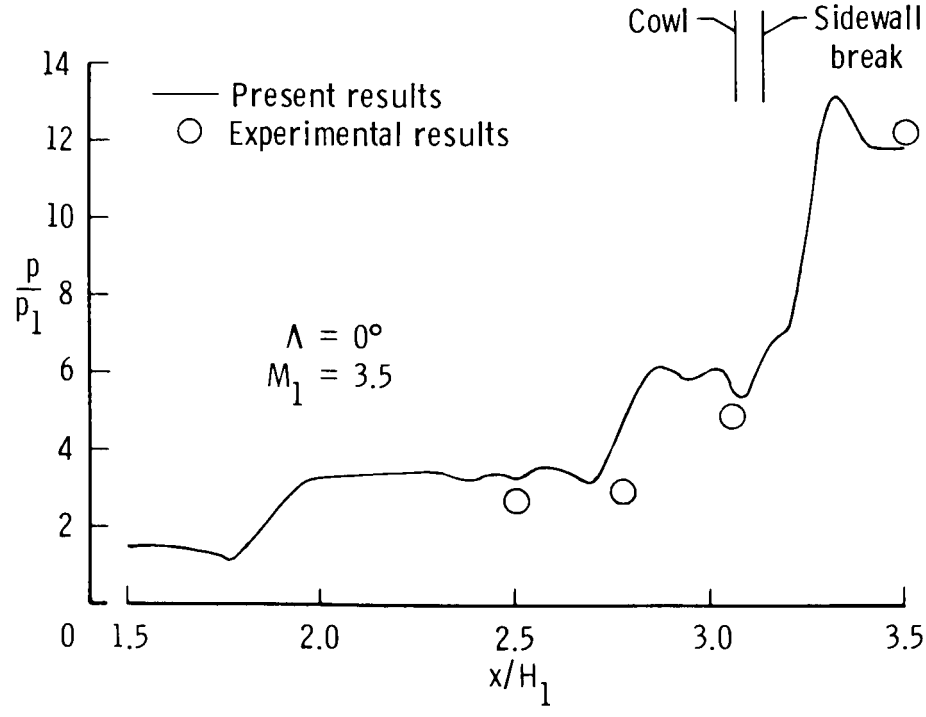

Figure 14.- Sidewall pressure distribution at $z/H_1 = 0.14$.

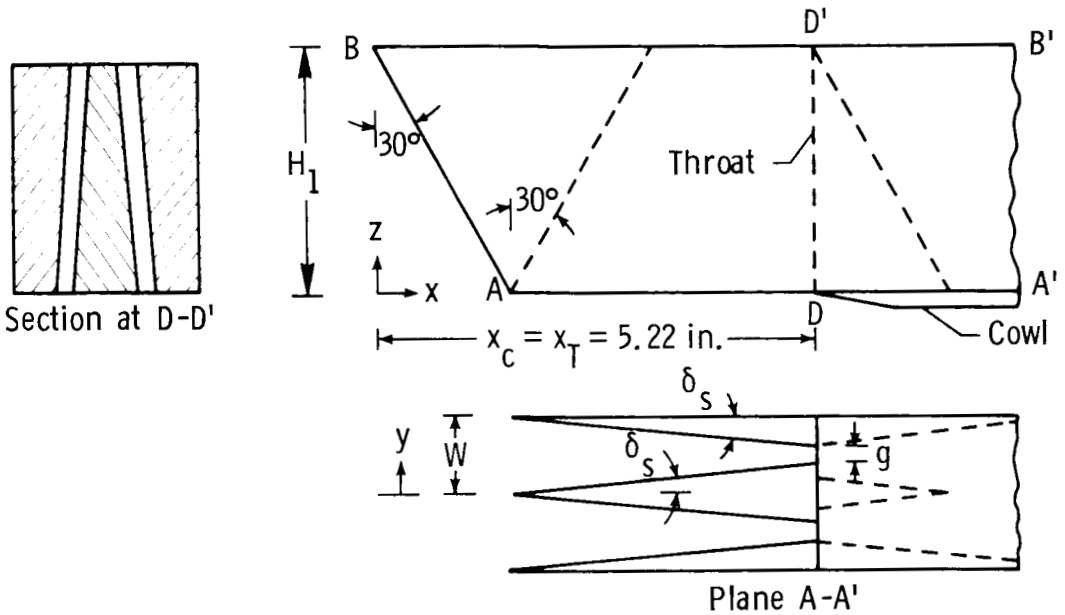

Figure 15.- Geometry of one-strut, reverse-sweep inlet. H_1 = 2.75 in.; W = 1.005 in.; W/g = 4.16; δ_s = 6°.

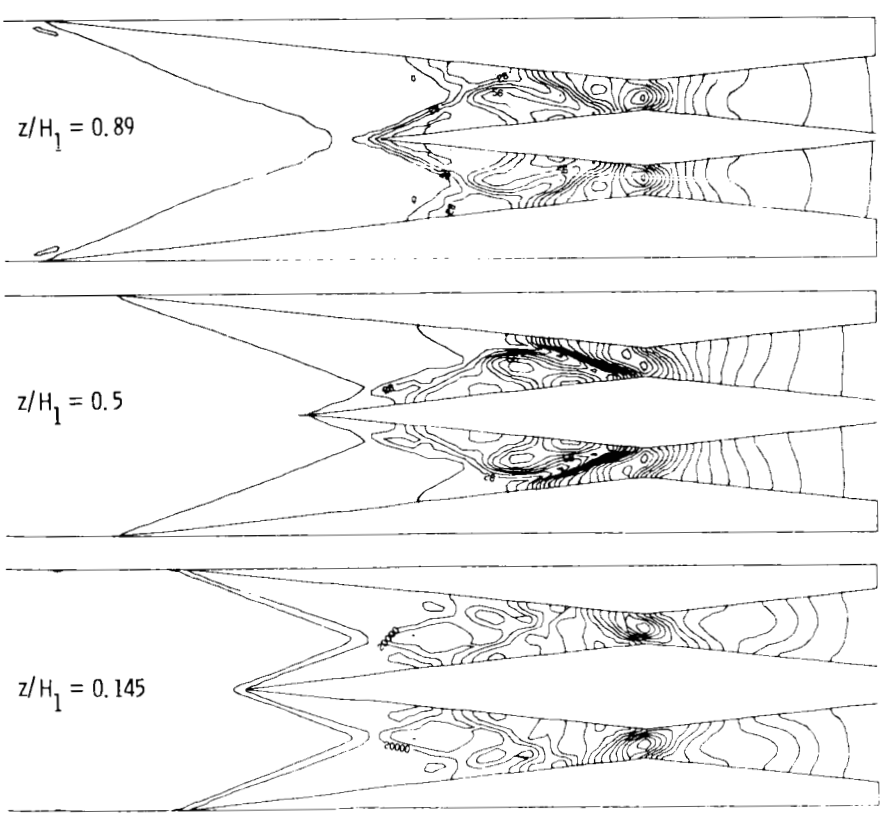

Figure 16.- Pressure contours in planes parallel to cowl plane.

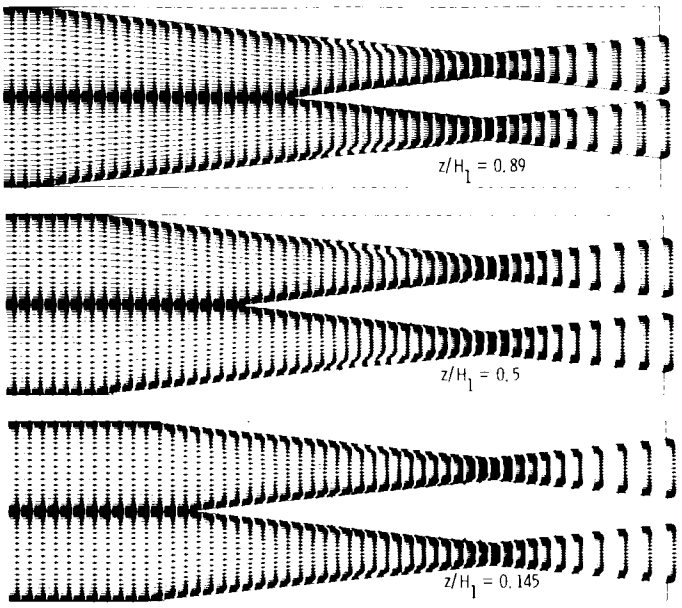

Figure 17.- Velocity vector field in planes parallel to cowl plane.

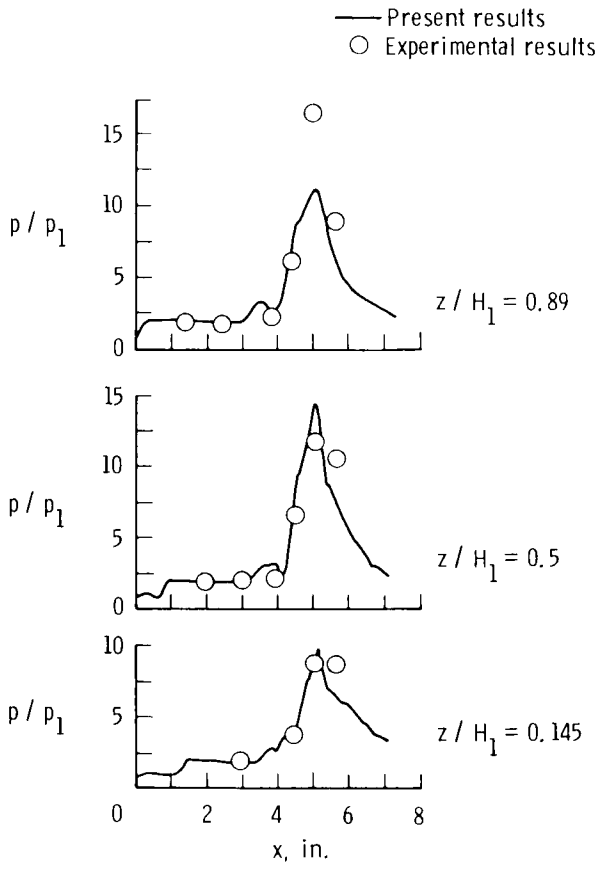

Figure 18.- Sidewall pressure distributions.

1. Report No.	2. Government Accession No.	3. Recipient's Catalog No.
NASA TP-2517		

4. Title and Subtitle	5. Report Date
Numerical Simulation of Scramjet Inlet Flow Fields	May 1986
	6. Performing Organization Code 505-31-03-02
7. Author(s) Ajay Kumar	8. Performing Organization Report No. L-16000
	10. Work Unit No.
9. Performing Organization Name and Address NASA Langley Research Center Hampton, VA 23665-5225	11. Contract or Grant No.
	13. Type of Report and Period Covered Technical Paper
12. Sponsoring Agency Name and Address National Aeronautics and Space Administration Washington, DC 20546-0001	14. Sponsoring Agency Code

15. Supplementary Notes

16. Abstract

A computer program has been developed to analyze supersonic combustion ramjet (scramjet) inlet flow fields. The program solves the three-dimensional Euler or Reynolds averaged Navier-Stokes equations in full conservation form by either the fully explicit or explicit-implicit, predictor-corrector method of MacCormack. Turbulence is modeled by an algebraic eddy-viscosity model. The analysis allows inclusion of end effects which can significantly affect the inlet flow field. Detailed laminar and turbulent flow results are presented for a symmetric-wedge corner, and comparisons are made with the available experimental results to allow assessment of the program. Results are then presented for two inlet configurations for which experimental results exist at the NASA Langley Research Center.

17. Key Words (Suggested by Author(s))	18. Distribution Statement
Hypersonic propulsion Scramjet inlet Euler and Navier Stokes equations	FEDD Distribution Subject Category 02

19. Security Classif. (of this report)	20. Security Classif. (of this page)	21. No. of Pages	22. Price
Unclassified	Unclassified	27	

Available: NASA's Industrial Applications Centers

NASA-Langley, 1986